DATA.AIR Gen 1

Description of Technology

Document No. GHG-21850-6101

23 January 2025

GHGSAT PRODUCT/DOCUMENT APPROVAL

Title:	**DATA.AIR Gen 1** **Description of Technology**
Document No.:	**GHG-21850-6101-c**
Submission Date:	**23 January 2025**
Contact Information:	GHGSat Inc. 1130 rue Sherbrooke Ouest, 15ème étage, Montréal, Québec, Canada, H3A 2M8 info@ghgsat.com +1 438 500 6700

CHANGE HISTORY

Version	Release Date	Notes
a	30 May 2024	Initial submission
b	6 September 2024	Revision
c	23 January 2025	Revision

CONTENT

Acronyms

F-P	Fabry-Pérot
FSR	Free Spectral Range
GIS	Geographic Information System
GHG	Greenhouse Gas
GSD	Ground Sampling Distance
GSM	Gyro Stabilized Mount
LFM	Linear Forward Model
OSF	Order Sorting Filter
TOASR	Top Of Atmosphere Spectral Radiance
WAF-P	Wide Angle Fabry-Pérot

1 TECHNOLOGY OVERVIEW

GHGSat provides remote sensing of methane emissions, based on the principle of optical absorption spectroscopy. Broadband light from the sun traverses the atmosphere, is backscattered by the ground, travels back up, and is then collected by the instrument. Methane absorbs specific wavelengths of the light, a spectral signature defined by molecular vibrational energy levels. A reduction in the light intensity at those wavelengths compared to a normal atmosphere indicates the presence of excess methane. Our spectrometers target methane absorption features in the shortwave infrared (SWIR) portion of the electromagnetic spectrum.

Instruments can be carried by microsatellites (DATA.SAT) or small aircrafts (DATA.AIR), which survey the target facilities as they orbit or fly above them. Both platforms share the same core of technology and processing methods. This document focuses on airborne instruments, which are flown at a typical elevation of 10,000 ft above ground level, providing a swath width of around 750 m. They operate in "nadir" mode, continuously capturing images while their line-of-sight points downwards.

The measurement concept is illustrated in Figure 1. Instruments are based on a wide-angle Fabry-Perot (WAF-P) imaging concept (Jervis et al., 2021; James J. Sloan et al., 2016). The WAF-P element consists of two optical flats mounted within a mechanical enclosure, with the two optical surfaces positioned such that the inner surfaces form an optical cavity (Figure 1.a). This component acts as a wavelength bandpass filter (with possibly more than 1 transmitted mode) which depends on the angle of the light rays inside the cavity (Figure 1.b). During the observation sequence, the ground target traverses the field-of-view, sampling the full extent of the spectral information contained in the images (Figure 1.c).

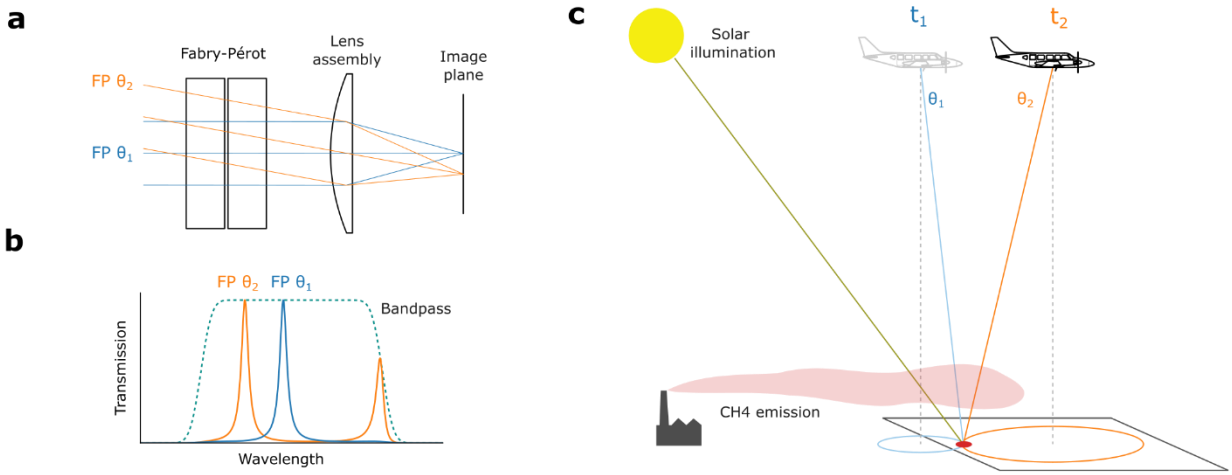

Figure 1. GHGSat DATA.AIR measurement concept. (a) Simplified representation of the optical system showing the FP element, lens, image plane, and light rays from two angles of incidence θ_1 and θ_2. (b) Transmission spectrum of the system for the two angles of incidence. (c) Measurement concept: a given location on the ground (red marker) is observed from different angles to provide information from different wavelengths.

The light intensity signal measured by the instrument can be converted to a methane concentration by using a variant of standard inverse methods. A mathematical forward model is constructed, which describes the wavelength-dependent transmission of light through the

atmosphere and the instrument, given a set of known state parameters (methane concentration, ground reflectance, F-P geometry, etc.). Nonlinear regression is then used to solve the inverse problem of retrieving the state parameters from measured light transmission. A spatially resolved methane concentration map is obtained from this algorithm, which is used to identify emissions which appear as high-concentration hotspots, and to calculate the emission rate. Example concentration maps measured by GHGSat DATA.AIR are provided in Figure 2 below, which shows two methane emissions from US oil & gas facilities.

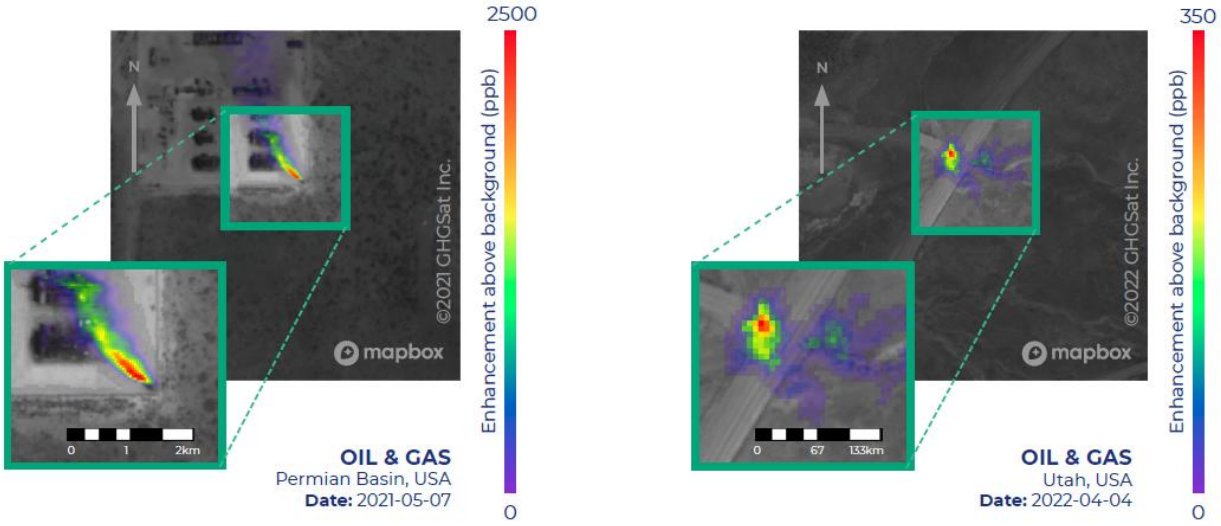

Figure 2. Sample methane concentration maps from GHGSat DATA.AIR for two US oil & gas facilities. Methane concentration enhancement above background is represented in colored heatmap, overlaid over standard aerial imagery.

2 DETAILED DESCRIPTION

This section is adapted from peer-reviewed publications describing the measurement technology: Jervis, D et al: The GHGSat-D imaging spectrometer, Atmos. Meas. Tech., 14, 2127–2140, 2021, and D. Varon et al, Atmos. Meas. Tech., 11, 5673–5686, 2018.

A separate *visual workflow* document is provided attached to this application and can be referenced to follow the flow of data and information through the processes described in some of the following sub-sections.

2.1 Measurement Concept

The GHGSat spectrometer is based on a wide-angle Fabry-Perot (WAF-P) imaging concept (James J Sloan et al., 2016). A programmable number of closely overlapping two-dimensional images are taken in which the atmospheric absorption spectrum is "imprinted" on the images in the form of spectral rings due to the angle-dependent Fabry-Perot transmission spectrum. During the observation sequence, the ground target traverses the field-of-view, sampling the full extent of the spectral information contained in the images.

Figure 3 illustrates how the F-P samples the backscattered solar radiance spectra to generate spectral rings in the image. Multiple F-P transmission modes are allowed through the OSF bandpass. Because the F-P transmission function depends only on θ, it is circularly symmetric and so can be expressed as a function of radius $r = \sqrt{(i - i_0)^2 + (j - j_0)^2}$. The $r = 0$ F-P transmission spectrum is shown in Figure 3(a) alongside the OSF transmission function and the normalized backscattered spectral radiance observed by the instrument (referred to as top-of-atmosphere spectral radiance or TOASR). For larger radii – and thus larger θ – the F-P spectrum shifts to lower wavelength with a $\cos(\theta)$ dependence, allowing us to sample different regions of the TOASR. Figure 3(b) shows the location (in wavelength space) of the F-P transmission peaks as a function of radius overlaid on the normalized TOASR. The instrument signal is shown in Figure 3(c) and the sensitivity of this signal to a change in methane vertical column density is shown in Figure 3(d). At each radius, the signal on the detector array is the wavelength integral of the TOASR multiplied by the F-P and OSF transmission spectra, i.e. the result of integrating Figure 3(b) along the vertical axis. A mathematical description of the forward model is given in Sect. 2.4.

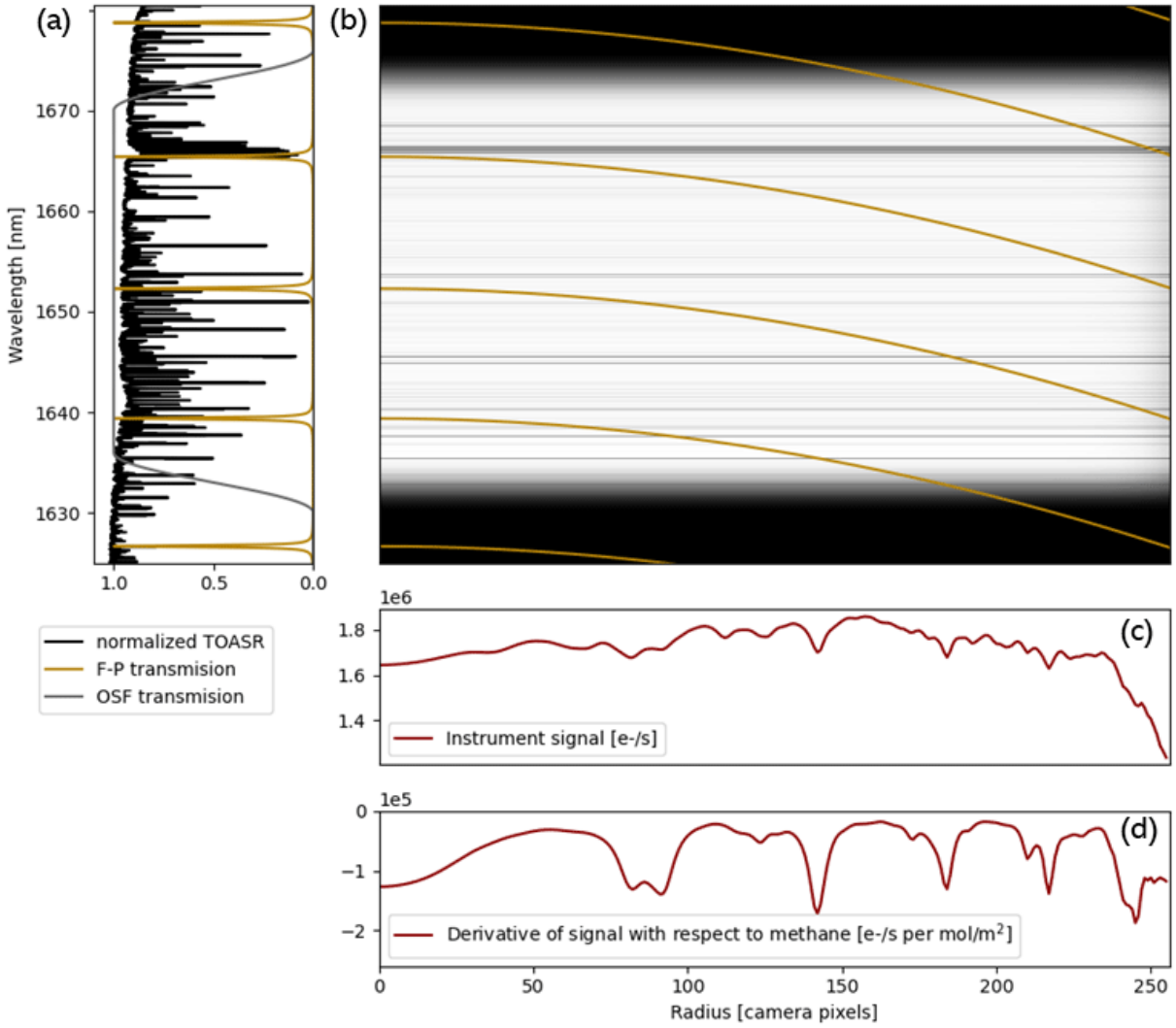

Figure 3: The plots (a) and (b) illustrate how the instrument signal in (c) is produced. In (a), the F-P and OSF transmission spectra are shown alongside the normalized top-of-atmosphere spectral radiance (TOASR) for the case of light rays incident on the F-P at normal incidence (i.e. $(\boldsymbol{r}, \boldsymbol{\theta}) = \mathbf{0}$). In (b), the location of the F-P transmission peaks are shown as a function of radius (gold lines) overlaid on the normalized TOASR (grey-scale background image). The horizontal dark bands at the top and bottom of (b) illustrate wavelengths where the OSF transmission is reduced to zero. By sampling a continuum of incident angles $\boldsymbol{\theta}$, the transmitted F-P transmission peaks measure a continuum if wavelengths within the passband. The instrument signal (c) results from integrating the multiplied signals in (b) along the vertical (wavelength) axis. The change in instrument signal with respect to a change in the methane vertical column density is plotted in (d). The TOASR and instrument signal are calculated assuming a target elevation at sea level, a solar zenith angle of $40°$, and vertical column densities of 0.68 mol m^{-2} (methane), 160 mol m^{-2} (CO_2), and 830 mol m^{-2} (water vapor).

In order to measure the spectrum of solar radiation backscattered from a specific ground cell, the location of the ground cell in each image must be known. This is done with an image co-registration algorithm. We then construct a spectrum for each ground cell along the image frame axis by recording the measured signal as a function of the ground cell's radial position with respect to the spectral ring center. Figure 5 (a)-(d) show an observation where the location of an example ground cell has been tracked in each frame. The constructed spectrum is shown in Figure 5 (e). The color of the data point represents the image frame from which the data was obtained. We construct approximately 200,000 of these spectra in order to retrieve the methane column density for each ground cell within the retrieval domain.

2.2 Instrumentation

The GHGSat instrument optical system (Figure 4) is composed of three lens assemblies with focal lengths f_{t1}, f_{t2}, and f_{im}: the first two lenses, in confocal arrangement, constitute the telescope. The last lens, the imaging assembly, forms a two-dimensional image of the ground on the detector. The F-P is placed in the Fourier plane of the optical system, between f_{t2} and f_{im}. An order sorting filter (OSF), placed between the lenses that make up the f_{t2} assembly, defines the spectral bandpass region. The choice of focal lengths must balance several considerations simultaneously. First, the angular magnification ratio of the telescope $|f_{t1}/f_{t2}|$ must be consistent with the mechanical constraints on input aperture and F-P size, and the spectroscopic constraints that dictate the desired range of incident ray angles on the F-P. Second, the effective focal length $f = f_{im}|f_{t1}/f_{t2}|$ is constrained by the choice of spatial resolution.

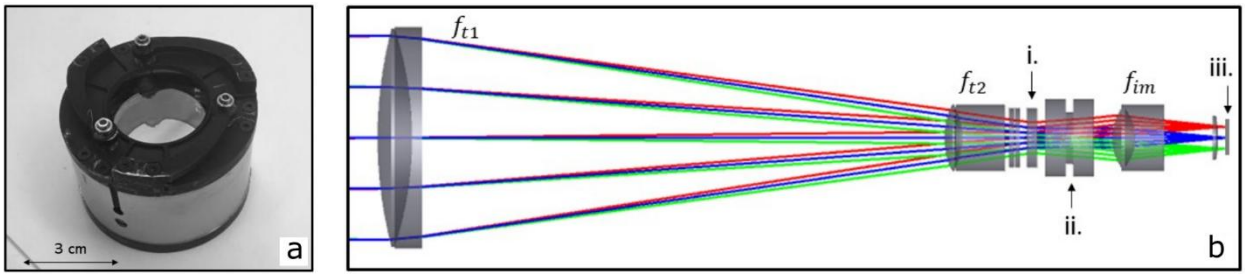

Figure 4: (a) The mounted Fabry-Perot interferometer. (b) Schematic of the unfolded optical system with the i.) OSF, ii.) F-P, and iii.) detector identified. The red, blue, and green rays originate from different ground locations.

For a given image, a polychromatic light ray originating from a specific ground location enters the optical system through the input aperture at some angle pair (ψ, ϕ), where ψ is the small elevation angle and ϕ is the azimuthal angle. In the paraxial approximation, the light ray emerges from the telescope with angle pair $(\left|\frac{f_{t1}}{f_{t2}}\right| \psi, \phi)$ and is incident on the F-P. The imaging assembly then focuses the light ray to detector pixel

$$(i, j) = (i_0 + b\left(\left|\frac{f_{t1}}{f_{t2}}\right| \psi\right) \cos(\phi), j_0 + b\left(\left|\frac{f_{t1}}{f_{t2}}\right| \psi\right) \sin(\phi)), \quad (1)$$

where b is a proportionality constant relating angle to pixel radius. The optical axis intercepts the 1280 x 1024 temperature controlled InGaAs detector array at pixel (i_0, j_0).

The GHGSat instrument F-P element consists of two optical flats mounted within a mechanical enclosure. The two optical surfaces are positioned such that the inner surfaces, with reflectivity R and spaced a distance d apart, form an optical cavity. Light with wavelength λ and incident angle $\theta = \left|\frac{f_{t1}}{f_{t2}}\right| \psi$ with respect to the F-P surface normal is transmitted according to:

$$T_{FP}(\theta,\lambda) = \frac{1}{1+\left(\frac{2\mathcal{F}}{\pi}\right)^2 \sin^2\left(\frac{2\pi n d\cos(\theta)}{\lambda}\right)} \quad (2)$$

where n is the index of refraction of the medium within the optical cavity and $\mathcal{F} = \pi\sqrt{R}/(1-R)$ is the reflectivity finesse. For each value of θ, the transmission spectrum of the F-P is a series of peaks that are spaced in wavelength by the free spectral range $FSR = \lambda^2/(2d)$ with a spectral width characterized by the full-width half-maximum $FWHM = FSR/\mathcal{F}$. Because the F-P accepts a continuum of θ values it samples a continuum of wavelengths within the passband.

In applications using F-P based spectrometers, the F-P gap spacing d is often dynamically scanned during the measurement (Reay et al., 1974). In contrast, the GHGSat instrument uses a fixed gap spacing and exploits the angular dependence of the m^{th} F-P transmission mode's spectral position $\lambda_m = 2\pi n d\cos(\theta)/m$ to measure the spectrum of the incident light. This approach simplifies the mechanical design and makes it much easier to meet stringent stability requirements. The FSR is chosen so that there are enough F-P transmission modes within the spectral bandpass to sample the entirety of the spectral bandpass within the imaging field of view. The F-P is temperature-controlled to keep thermal mechanical drift to a minimum.

The airborne sensors (DATA.AIR) can be mounted in any appropriate third-party aircraft and deployed with an operator as required for aerial survey campaigns. Any aircraft selected for surveying must have a camera port to accommodate the instrument.

The imaging spectrometer is installed in nadir viewing configuration. The mounting assembly includes passive vibration dampers and a commercial motorized gyro-stabilized mount (GSM), which isolate the optical system orientation from the aircraft and provides uniform viewing angle throughout each flight line. In addition, the position and attitude of the instrument are tracked by an inertial navigation system (INS) which includes a global positioning system (GPS), gyroscopes and accelerometers.

Some key instrument and survey parameters are summarized in Table 1.

Table 1: Instrument and operational parameters

Parameter	Value	Comments
Spectral range	~1.6 – 1.7 µm	Exact range within these bounds
Spectral sampling	0.0001 – 0.1 nm/pixel	Spectral sampling is nonlinear across the detector due to F-P transmission mode behaviour. Spectral sampling is finer near the center of the detector and coarser at greater radii.
Ground sampling distance (GSD)	~1.5 m	Depends on altitude and viewing angle
Transverse field of view	~750 m	Illuminated portion of each circular frame defines the swath width
Flight altitude (Above ground level)	~10,000 ft	

2.3 Retrieval Method

The goal of the retrieval algorithm is to estimate the instrument and atmospheric state vector $\mathbf{x}$ from a measurement vector $\boldsymbol{y}$. This is done by constructing a combined forward model $\boldsymbol{F}(\mathbf{x})$ of the instrument and atmosphere and making the association:

$$\boldsymbol{y} = \boldsymbol{F}(\mathbf{x}) + \boldsymbol{\epsilon}_y + \boldsymbol{\epsilon}_F \tag{3}$$

where $\boldsymbol{\epsilon}_y$ represents the measurement error and $\boldsymbol{\epsilon}_F$ represents error in the forward model. A retrieval of $\mathbf{x}$ requires that we have accurate knowledge of both the forward model and the errors in the measurement system. Because $\boldsymbol{F}(\mathbf{x})$ is a nonlinear function of $\mathbf{x}$, we must solve for the state vector iteratively. This requires knowledge of the Jacobian $\boldsymbol{K}(\mathbf{x}) = \frac{\partial \boldsymbol{F}(\mathbf{x})}{\partial \mathbf{x}}$ to weight the state vector step $\boldsymbol{\Delta}\mathbf{x}^i$ taken during the i^{th} iteration. In this section, we describe the instrument and atmospheric forward model and outline the inversion procedure used to estimate $\mathbf{x}$.

2.4 Forward Model

The forward model represents our best knowledge of the instrument and atmosphere, with approximations used to evaluate the model more efficiently when performing retrievals. The camera signal $F_{i,j}$ at detector pixel (i,j) in photocurrent units [$e^- s^{-1}$] is given by:

$$F_{i,j}(\mathbf{x}) = \int L(\mathbf{x},\lambda) \cdot C(\lambda) \cdot QE(\lambda) \cdot T_{OSF}(\lambda) \cdot T_{FP}(\theta,\lambda) d\lambda \tag{4}$$

where $L(\mathbf{x},\lambda)$ is the spectral radiance as a function of the state parameter $\mathbf{x}$ and wavelength λ, $C(\lambda)$ is the radiometric conversion factor that converts spectral radiance to the number of photons on a pixel per unit time, $QE(\lambda)$ is the quantum efficiency with which the camera converts a photon to electric charge, $T_{OSF}(\lambda)$ is the transmission of the order-sorting filter that defines the spectral bandpass region, and $T_{FP}(\theta,\lambda)$ is the F-P transmission function defined in Eq. (2). The camera signal in Eq. (4) is plotted as a function of radius in Figure 5 (c).

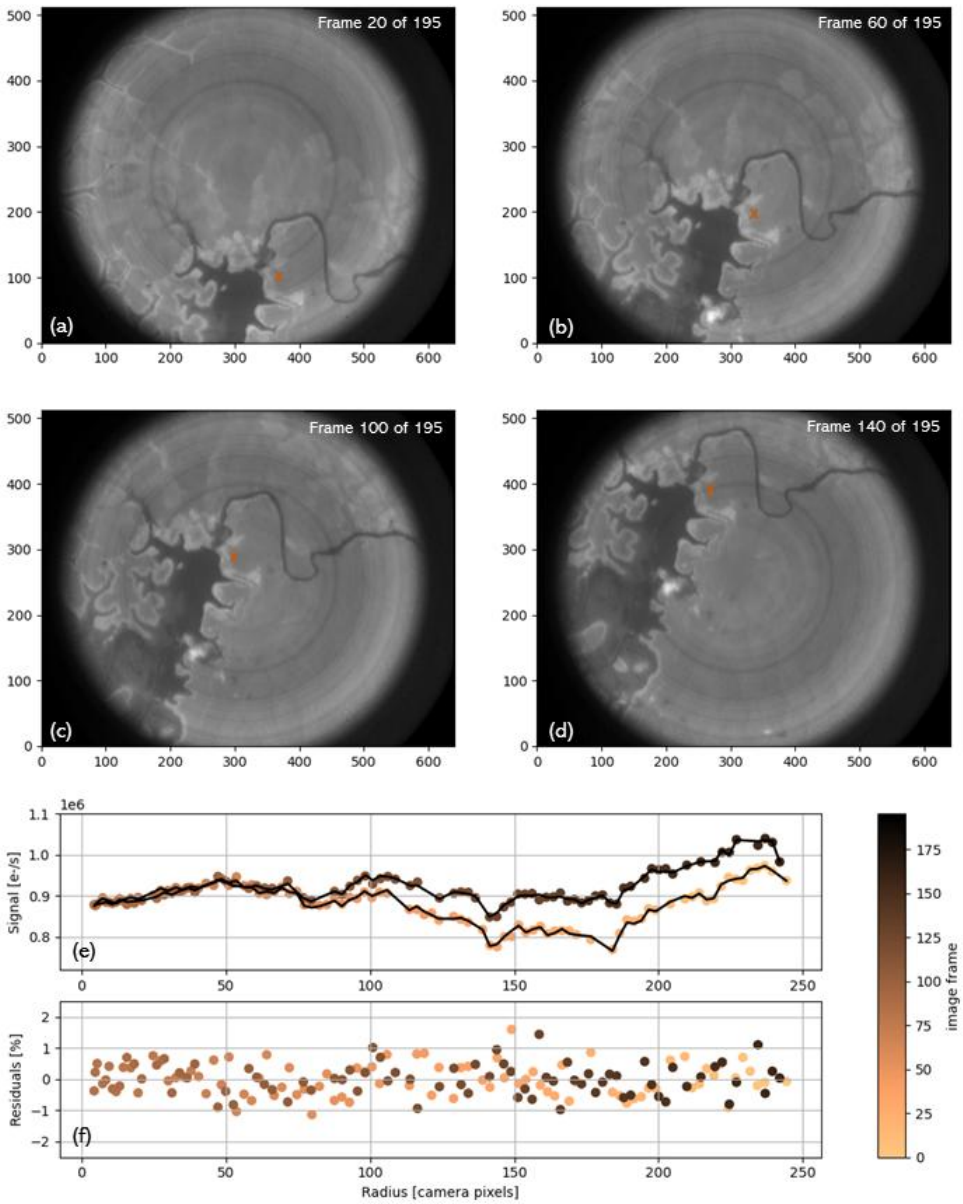

Figure 5. The images (a), (b), (c)., and (d). show a selection of frames from a satellite observation over the Lom Pangar hydroelectric reservoir in Cameroon taken on April 20th, 2017 with an example ground location (denoted by an orange "x") tracked in each frame. The same measurement concept is applicable to DATA.AIR acquired from an aircraft. The image axes are in pixels, with each pixel representing a 24 x 24 m² area on the ground. The plot in (e) shows the signal (circles) from the example ground location as a function of the image frame (circle colour) and radius from spectral ring center (horizontal axis). The forward model (black line) is plotted alongside the signal data and residuals between model and data are shown in (f).

2.5 Atmospheric Model

The spectral radiance $L(\mathbf{x}, \lambda)$ is calculated from the spectral irradiance $I(\lambda)$ assuming Lambertian surface reflectance:

$$L(\mathbf{x},\lambda) = \frac{a(\lambda)\cdot\cos(\theta_{sza})}{\pi R_{E-S}^2} I(\mathbf{x}',\lambda) \quad (5)$$

where $a(\lambda)$ is the spectrally-dependent surface albedo, θ_{sza} is the solar zenith angle, R_{E-S} is the relative Earth-Sun distance, $\mathbf{x}'$ is the state parameter vector without the albedo, and the spectral irradiance is the solution to a simplified radiative transfer equation where thermal emission, aerosol and molecular scattering have been neglected (Chandrasekhar, 2013):

$$\mu \frac{\partial I(\mathbf{x}',\lambda)}{\partial z} = -\alpha_{abs} I(\mathbf{x}',\lambda). \quad (6)$$

This equation is integrated along the downwelling and upwelling light path. Here $\mu = \cos(\theta)$, θ is the angle that the light travels through the atmosphere with respect to the Earth's surface normal, z is the altitude, α_{abs} is the pressure, temperature, wavelength, and species dependent absorption coefficient calculated using the HITRAN API (Kochanov et al., 2016), and the solar irradiance is introduced through a boundary condition and generated from the AER solar irradiance model (Clough et al., 2005). We integrate the radiative transfer equation discretely assuming 100 atmospheric layers that are evenly spaced in pressure.

We justify excluding thermal emission and molecular scattering from the atmospheric model because both are small effects for the wavelengths within our spectral bandpass region. Previous studies of simulated carbon dioxide retrievals using only the 1563 - 1585 nm band have found that neglecting aerosol and molecular scattering can lead to a few percent error, depending on the surface albedo and aerosol optical depth (Aben et al., 2007). This error can be either positive or negative, depending on whether the presence of aerosols – in combination with the surface albedo - leads to an increase or decrease in the average optical pathlength. An analysis of SCIAMACHY retrievals in this same spectral region found that errors decrease for aerosol vertical distributions that are narrow and closer to the Earth's surface (Houweling et al., 2005). GHGSat retrievals are primarily intended to measure local plume enhancements. Therefore, we are especially concerned with any unmodeled effects with spatial structure on the length scales of emission plumes. This could potentially include aerosol scattering, such as aerosols that might conceivably be co-emitted with methane plumes. However, since the presence of these aerosol plumes would be much closer to the surface and narrower in vertical profile than the aerosol profiles retrieved in (Aben et al., 2007; Houweling et al., 2005), we expect that errors arising from neglecting scattering should be small compared with other sources of measurement error, similar to what is assumed in AVIRIS airborne methane retrievals (Thorpe et al., 2014). We also note a recent study in which the effect of neglecting aerosols in an AVIRIS airborne methane plume retrieval was shown to be < 5% for representative methane plume enhancements and a significant aerosol optical depth (Huang et al., 2020).

2.6 Inversion Procedure

For any ground cell (p,q) in a reference frame we can compare the observation data vector $\mathbf{y}^{(pq)} = \{y_{i_1,j_1}^{(pq)}, y_{i_2,j_2}^{(pq)}, \ldots, y_{i_k,j_k}^{(pq)}\}$ to the forward model vector $\mathbf{F}(\mathbf{x}^{(pq)}) = \{F_{i_1,j_1}(\mathbf{x}^{(pq)}), F_{i_2,j_2}(\mathbf{x}^{(pq)}), \ldots, F_{i_k,j_k}(\mathbf{x}^{(pq)})\}$ and infer the state vector $\mathbf{x}^{(pq)}$ using a variant of standard inverse methods described below. The subscripts refer to the pixel indices for this ground cell within the respective frames of the image sequence from 1 to k. The reference frame coordinate system can then be georeferenced with the appropriate rotational and scale transformation.

We use optimal estimation (Rodgers, 2000) to infer the posterior distribution of the state vector given the observation data, an error model, and a prior distribution for the state vector. Assuming a Gaussian form for the measurement and prior probability density functions, maximizing the joint probability density function amounts to minimizing the cost function:

$$\chi^2(\mathbf{x}) = \left(\mathbf{y} - \boldsymbol{F}(\mathbf{x})\right)^{\mathrm{T}} \mathbf{S_o^{-1}} \left(\mathbf{y} - \boldsymbol{F}(\mathbf{x})\right) + (\mathbf{x} - \mathbf{x}_a)^{\mathrm{T}} \mathbf{S_a^{-1}} (\mathbf{x} - \mathbf{x}_{\mathrm{a}}) \tag{7}$$

where $\mathbf{S_o}$ is the observation error covariance matrix, $\mathbf{S_a}$ is the prior covariance matrix, and $\mathbf{x}_{\mathrm{a}}$ is the prior state vector. The Gauss-Newton procedure for minimizing the cost function requires that we update the state vector at each iteration by a step:

$$\Delta\mathbf{x}^{i+1} = (\boldsymbol{K}^{\mathrm{T}}(\mathbf{x}^i)\mathbf{S_o^{-1}}\boldsymbol{K}(\mathbf{x}^i) + \mathbf{S_a^{-1}})^{-1} \left(\boldsymbol{K}^{\mathrm{T}}(\mathbf{x}^i)\mathbf{S_o^{-1}} \left(\mathbf{y} - \boldsymbol{F}(\mathbf{x}^i)\right) + \mathbf{S_a^{-1}}(\mathbf{x} - \mathbf{x}_{\mathrm{a}})\right) \tag{8}$$

where $\boldsymbol{K}(\mathbf{x}^i)$ is the Jacobian of the forward model evaluated at $\mathbf{x}^i$.

At each iteration of the Gauss-Newton procedure, the forward model and Jacobian must be evaluated. This is computationally expensive for a single cell and evaluating it for the ~200,000 ground cells in our field-of-view is impractical. Instead, we use a two-step procedure: (1) a scene-wide average retrieval using the full forward model to estimate the scene-wide average state vector $\hat{\mathbf{x}}$, and (2) a per-cell retrieval done using a linearized forward model (LFM) evaluated at the linearization point $\hat{\mathbf{x}}$. The separate retrieval steps are described in the following sections. As a note, full flight lines can consist of an arbitrarily large number of frames. For retrievals, they are broken down into overlapping "chunks" of around 200 frames which are processed independently.

2.7 Scene-wide Retrieval

The goal of the scene-wide retrieval is two-fold: to retrieve scene-wide averaged surface and atmospheric parameters such as albedo and molecular column density, and to retrieve the F-P gap spacing. Even though the F-P is thermally stabilized, residual drift in the F-P gap spacing can occur during a survey. Because the F-P gap spacing directly affects the signal on each detector pixel, we retrieve d for each chunk. The scene-wide retrieval uses the full instrument model $F_{i,j}(\mathbf{x})$ from Eq. (4) in the optimal estimation procedure. The data vector $\mathbf{y}$ in the scene-wide retrieval is the radial average of the average of all image frames. The result of the scene-wide retrieval is the state parameter estimate $\hat{\mathbf{x}}$ which includes retrieved instrument parameters and the scene-wide averaged methane column density.

2.8 Spatially Resolved Column Retrieval

A linearized forward model (LFM) is constructed at the linearization point $\hat{\mathbf{x}}$:

$$\mathbf{F}^{LFM}\left(\mathbf{x}^{(pq)}\right) = \mathbf{x}^{(pq)}(1)\left(\mathbf{K}_1(\hat{\mathbf{x}}) + \frac{1}{\hat{\mathbf{x}}(1)}\sum_{l=2}^{n}\mathbf{K}_l(\hat{\mathbf{x}})\left(\mathbf{x}^{(pq)}(l) - \hat{\mathbf{x}}(l)\right)\right) + \sum_{l=n}^{n+m}\mathbf{K}_l(\hat{\mathbf{x}})\left(\mathbf{x}^{(pq)}(l) - \hat{\mathbf{x}}(l)\right) \tag{9}$$

where the first element of the state vector is taken to be the surface reflectance. The methane column density enhancement and ground reflectance model parameters are retrieved for each ground cell (p, q). Here, we set the prior variances to be very large such that the retrieved parameters are almost entirely determined by the data. There are two terms in the LFM: one with n terms that includes state parameters whose Jacobians scale with the surface reflectance (for example the molecular column densities), and another with m terms for state parameters whose Jacobians are not scaled by the reflectance. In particular, the molecular components of the Jacobian are calculated using a column density enhancement in the lowest atmospheric layer that extends from the surface to approximately 100 m altitude. The primary advantage of using the LFM is that we only compute the forward model and Jacobians once at the beginning of the per-cell retrieval. A disadvantage is that for the parameters that are nonlinear in the forward model, a retrieval using the LFM will introduce systematic biases for deviations far from the linearization point. For the particular case of molecular column densities, this leads to an underestimation that is corrected in post-processing using a non-linear correction function determined from a comparison of $\mathbf{F}^{LFM}(\mathbf{x})$ with $\mathbf{F}(\mathbf{x})$ at the appropriate linearization point (D J Varon et al., 2019).

2.9 Emissions Identification

Emissions are identified by visual inspection of the spatially resolved methane density retrieved at the previous step. Emissions are mostly identified based on the strength of the methane enhancement relative to the uncertainty (high signal to error ratio). To distinguish real methane enhancements from noise and artifacts, the operator assesses the spatial structure of the plume (general morphology, alignment with the wind direction), and ensures the enhancement is not correlated with features present in the albedo or its gradient. Knowledge of the infrastructure (or lack-thereof) also factors in the decision process, which can come from customer-provided site lists and by inspection of the albedo field or standard satellite imagery of the surveyed sites. All identified emissions and uncertain cases are reviewed by a second GHGSat operator to provide quality assurance against false positives.

When an emission is detected, the operator identifies its origin based on wind direction, plume morphology, and location of potentially emitting infrastructure. Additionally, a binary mask of the plume is computed using an algorithm based on image filtering, thresholding, and a flood-fill algorithm described in the supplementary information (SI) document. This mask identifies which connected ground cells have a methane concentration above the measurement uncertainty and originate from the defined source.

2.10 Emission Rate Retrieval

The methane emission rate is calculated using the method of integrated mass enhancement (IME) (Varon et al., 2018). IME is defined as the total amount of detectable methane enhancement that originates from a given source. For an observed plume comprising N ground cells of area A_j ($j = 1 \dots N$) and column density enhancement $\Delta\Omega_j$ (output of step 2.8),

$$\mathrm{IME} = \sum_{j=1}^{N} \Delta\Omega_j A_j \tag{10}$$

IME measures the local accumulation of methane, which is driven by two factors: the emission rate Q, and the rate at which the methane dissipates in the surrounding atmosphere characterized by its residence time τ. One can express τ dimensionally in terms of an effective wind speed U_{eff} [m s^{-1}] and a plume size L [m]:

$$Q = \frac{1}{\tau}\mathrm{IME} = \frac{U_{\mathrm{eff}}}{L}\mathrm{IME} = \frac{U_{\mathrm{eff}}}{L}\sum_{j=1}^{N} \Delta\Omega_j A_j \tag{11}$$

U_{eff} and L would have simple physical meanings of wind speed and plume length if dissipation of the plume occurred by uniform transport to a terminal distance downwind of the source. But the actual mechanism for plume dissipation is turbulent diffusion, which takes place in all directions. U_{eff} and L must therefore be viewed as operational parameters to be related to observations of wind speed U and plume extent. These relationships take the following empirical form:

$$L = \sqrt{A_M} \tag{12}$$

$$U_{\mathrm{eff}} = \alpha_1 \, \mathrm{U}_{10} + \alpha_2 \tag{13}$$

In the equations above: A_M is the area of the plume mask (connected ground cells where the enhancement is above the measurement uncertainty level); U_{10} is the wind speed at 10 m above ground, obtained from a third-party weather provider; α_1 and α_2 are model parameters inferred from controlled releases. More information on the source rate calculation is provided in the SI document and in (Varon et al., 2018).

3 LIMITATIONS

The measurement technique has limitations that are inherent to passive optical absorption spectroscopy. In particular:

- Measurements during the night or in overcast weather are not possible. In partly cloudy conditions, obscured areas with insufficient signal will be flagged as invalid.
- Offshore measurements require a specific observing configuration to capture the direct sun glint reflection (predominantly specular reflection as opposed to diffuse reflection on land). At this moment, GHGSat only provides offshore measurements from its satellite platform (DATA.SAT), and not for aerial surveys (DATA.AIR).
- Underground leaks can be detected after they reach the surface.

Variations in wind speed affect the sensitivity and quantification accuracy, because the local concentration of methane from a leak is driven not only by the emission rate, but also the rate at which wind dissipates methane in the surrounding atmosphere. High wind speeds increase the detection threshold. On the other end, very low wind speed will favor detection of small leaks, but makes quantification more difficult as the relative uncertainty of the emission rate is dominated by that of local wind. Both of those effects are accounted for in the methane quantification uncertainty.

Geographic and seasonal variability of the ground reflectance affects the amount of light collected by the instrument and therefore modulates the signal to noise ratio due to shot noise. For example, dry land tends to be more reflective than humid ones, or regions with heavy tree cover. Snow is also poorly reflective in the SWIR band. Such conditions are not excluded from commercial operations but will result in higher measurement uncertainty.

In addition to average reflectance effects described above, retrieved methane concentration can be spatially correlated with ground reflectance, resulting in some degree of systematic noise in the measurement. Scenes with uniform reflectance therefore allow a better precision and lower detection threshold than heterogeneous ones including mountains, urban scenes, or areas with a complex topography. Such effects are also accounted for in the measurement error.

It is worth noting that reflectance effects, both via shot noise and correlated noise, matter mostly in a short range (tens of meters) around potential methane-emitting facilities, where a plume would be located.

Finally, other gas species (CO2, water vapor) do not interfere in a significant way with CH4 measurements. The main reasons are (1) the GHGSat instruments use a narrow spectral band which is largely dominated by methane absorption lines, and (2) the weak absorption lines of other species do not overlap significantly with CH4 within the limit of spectral resolution. As a result, GHGSat does not restrict its operations with relative humidity conditions, provided that the sun is not covered.

4 REFERENCES

Aben, I., Hasekamp, O., Hartmann, W., 2007. Uncertainties in the space-based measurements of CO2 columns due to scattering in the Earth's atmosphere. J. Quant. Spectrosc. Radiat. Transf. 104, 450–459.

Chandrasekhar, S., 2013. Radiative transfer. Courier Corporation.

Clough, S.A., Shephard, M.W., Mlawer, E.J., Delamere, J.S., Iacono, M.J., Cady-Pereira, K., Boukabara, S., Brown, P.D., 2005. Atmospheric radiative transfer modeling: a summary of the AER codes. J. Quant. Spectrosc. Radiat. Transf. 91, 233–244.

El Abbadi, S., Chen, Z., Burdeau, P., Rutherford, J., Chen, Y., Zhang, Z., Sherwin, E., Brandt, A., 2023. Comprehensive evaluation of aircraft-based methane sensing for greenhouse gas mitigation. https://doi.org/10.31223/X51D4C

Houweling, S., Hartmann, W., Aben, I., Schrijver, H., Skidmore, J., Roelofs, G.-J., Breon, F.-M., 2005. Evidence of systematic errors in SCIAMACHY-observed CO 2 due to aerosols. Atmospheric Chem. Phys. 5, 3003–3013.

Huang, Y., Natraj, V., Zeng, Z., Yung, Y.L., 2020. Quantifying the impact of aerosol scattering on the retrieval of methane from airborne remote sensing measurements. Atmospheric Meas. Tech. Discuss. 1–28.

Jacob, D.J., Turner, A.J., Maasakkers, J.D., Sheng, J., Sun, K., Liu, X., Chance, K., Aben, I., McKeever, J., Frankenberg, C., 2016. Satellite observations of atmospheric methane and their value for quantifying methane emissions. Atmospheric Chem. Phys. 16, 14371–14396. https://doi.org/10.5194/acp-16-14371-2016

Jervis, D., McKeever, J., Durak, B.O.A., Sloan, J.J., Gains, D., Varon, D.J., Ramier, A., Strupler, M., Tarrant, E., 2021. The GHGSat-D imaging spectrometer. Atmospheric Meas. Tech. 14, 2127–2140. https://doi.org/10.5194/amt-14-2127-2021

Kochanov, R. V, Gordon, I.E., Rothman, L.S., Wcisło, P., Hill, C., Wilzewski, J.S., 2016. HITRAN Application Programming Interface (HAPI): A comprehensive approach to working with spectroscopic data. J. Quant. Spectrosc. Radiat. Transf. 177, 15–30.

Reay, N.K., Ring, J., Scaddan, R.J., 1974. A tunable Fabry-Perot filter for the visible. J. Phys. [E] 7, 673.

Rodgers, C.D., 2000. Inverse methods for atmospheric sounding: theory and practice. World scientific.

Rutherford, J., Sherwin, E., Chen, Y., Aminfard, S., Brandt, A., 2023. Evaluating methane emission quantification performance and uncertainty of aerial technologies via high-volume single-blind controlled releases. https://doi.org/10.31223/X5KQ0X

Sherwin, E.D., El Abbadi, S.H., Burdeau, P.M., Zhang, Z., Chen, Z., Rutherford, J., Chen, Y., Brandt, A., 2023a. Single-blind test of nine methane-sensing satellite systems from three continents. https://doi.org/10.31223/X56089

Sherwin, E.D., Rutherford, J.S., Chen, Y., Aminfard, S., Kort, E.A., Jackson, R.B., Brandt, A.R., 2023b. Single-blind validation of space-based point-source detection and quantification of onshore methane emissions. Sci. Rep. 13, 3836. https://doi.org/10.1038/s41598-023-30761-2

Sloan, James J, Durak, B., Gains, D., Ricci, F., McKeever, J., Lamorie, J., Mark, S., Latendresse, V., Lavoie, J., Kruzelecky, R., others, 2016. Fabry-Perot interferometer based satellite detection of atmospheric trace gases.

Thorpe, A.K., Frankenberg, C., Roberts, D.A., 2014. Retrieval techniques for airborne imaging of methane concentrations using high spatial and moderate spectral resolution: application to AVIRIS. Atmospheric Meas. Tech. 7, 491–506.

Varon, D.J., Jacob, D.J., McKeever, J., Jervis, D., Durak, B.O.A., Xia, Y., Huang, Y., 2018. Quantifying methane point sources from fine-scale satellite observations of atmospheric methane plumes. Atmospheric Meas. Tech. 11, 5673–5686. https://doi.org/10.5194/amt-11-5673-2018

Varon, D J, McKeever, J., Jervis, D., Maasakkers, J.D., Pandey, S., Houweling, S., Aben, I., Scarpelli, T., Jacob, D.J., 2019. Satellite discovery of anomalously large methane point sources from oil/gas production. Geophys. Res. Lett.